The timing of Start is determined primarily by increased synthesis of the Cln3 activator rather than dilution of the Whi5 inhibitor

Athanasios Litsios[a], Pooja Goswami[b], Hanna M. Terpstra[a], Carleton Coffin[b], Luc-Alban Vuillemenot[a], Mattia Rovetta[a], Ghada Ghazal[c], Paolo Guerra[a], Katarzyna Buczak[d], Alexander Schmidt[d], Sylvain Tollis[c,e,*], Mike Tyers[c,*], Catherine A. Royer[b,*], Andreas Milias-Argeitis[a,*], and Matthias Heinemann[a,*]

[a]Molecular Systems Biology, Groningen Biomolecular Sciences and Biotechnology Institute, University of Groningen, 9747 AG Groningen, Netherlands; [b]Biological Sciences, Rensselaer Polytechnic Institute, Troy, NY 12180; [c]Institute for Research in Immunology and Cancer, University of Montréal, Montréal, H3T 1J4 QC, Canada; [d]Proteomics Core Facility, Biozentrum, University of Basel, 4056 Basel, Switzerland; [e]Institute of Biomedicine, University of Eastern Finland, FI-70210 Kuopio, Finland

INTRODUCTION

How cells convert shallow-input gradients into all-or-none decisions is a fundamental problem in biology. Commitment to cell division is thought to require a threshold level of cell growth, but how incremental changes in growth are measured by the cell is unknown. Various hypotheses have been proposed to explain growth-dependent cell cycle commitment in late G1 phase in budding yeast (called Start), including two recent models. One model (Schmoller *et al.*, 2015) posits that as the nucleus grows during G1 phase, the nuclear concentration of the G1/S transcriptional inhibitor Whi5 slowly decreases, thereby increasing the probability of the Start transition. This model of passive dilution is predicated on estimates of Whi5 nuclear concentration as assessed by wide-field epifluorescence microscopy as a function of time in G1 phase daughter cells. An alternative model (Litsios *et al.*, 2019) posits that an increase in protein synthesis toward the end of G1 rapidly drives up the concentration of the highly unstable G1 cyclin Cln3, which activates Cdc28 (Cdk1), thereby triggering the phosphorylation-mediated dissociation of Whi5 from the SBF G1/S transcription factor complex and activation of the G1/S program. This model of active control of Start is supported by measurements of protein synthetic rate and Cln3 concentration as a function of time. Notably, based on wide-field epifluorescence detection of a Whi5-fluorescent protein (FP) fusion and mass spectrometry, Litsios *et al.* (2019) concluded that there is only "a small or no change in Whi5 concentration" throughout G1, consistent with earlier reported results (Dorsey *et al.*, 2018) using scanning Number and Brightness (sN&B) microscopy, a method that allows for determination of absolute protein concentrations.

In their Letter to *Molecular Biology of the Cell*, Schmoller *et al.* (2022) raise questions about the results and conclusions presented in our published studies (Dorsey *et al.*, 2018; Litsios *et al.*, 2019). Here, we respond to the criticisms of Schmoller *et al.* and demonstrate how wide-field fluorescence microscopy experiments to determine nuclear Whi5 concentration dynamics can be confounded by uncontrolled effects, which include photobleaching, partial confocal effects, and nuclear-to-cytoplasmic volume scaling. Further, we provide additional experimental evidence demonstrating that nuclear Whi5 concentration is essentially constant as cells grow in G1 phase and that Cln3 and protein synthesis dynamics occur as reported in Litsios *et al.* (2019). These results suggest that instead of being triggered by dilution of the stable inhibitor Whi5, Start is rather primarily controlled by the increase in protein synthesis rate in G1 and the concomitant production of the unstable activator Cln3.

RESULTS AND DISCUSSION

There is little or no change in Whi5 concentration during G1

It was originally proposed by Schmoller *et al.* (2015) that Whi5 concentration decreases during G1 and thereby triggers Start. This model is based on estimates of Whi5 concentration during G1 obtained by time-lapse wide-field fluorescence microscopy. In their Letter to *Molecular Biology of the Cell*, Schmoller *et al.* (2015) argue that normalization and alignment in time of single-cell Whi5 traces can mask the extent to which Whi5 is diluted.

DOI:10.1091/mbc.E21-07-0349

*Address correspondence to: Sylvain Tollis (sylvain.tollis@uef.fi); Mike Tyers (md.tyers@umontreal.ca); Catherine A. Royer (royerc@rpi.edu); Andreas Milias-Argeitis (a.milias.argeitis@rug.nl); Matthias Heinemann (m.heinemann@rug.nl).

Abbreviations used: ACN, acetonitrile; CDK, cyclin-dependent kinase; FLIM, fluorescence-lifetime imaging microscopy; FOV, field of view; FP, fluorescent protein; FRAP, fluorescence recovery after photobleaching; FWHM, full width at half-maximum; GFP, green fluorescent protein; LC, liquid chromatography; m/z, mass-to-charge; MS, mass spectrometry; OD, optical density; 1p, one-photon; 2p, two-photon; PRM, parallel-reaction monitoring; RFP, red fluorescent protein; SBF, Swi4/6 cell cycle box-binding factor; SC, synthetic complete; sfGFP, superfolder GFP; S/N, signal-to-noise; sN&B, scanning number and brightness; TCA, trichloroacetic acid; TCEP, tris(2-carboxyethyl)phosphine; TFA, trifluoroacetic acid; YPD, yeast extract peptone dextrose.

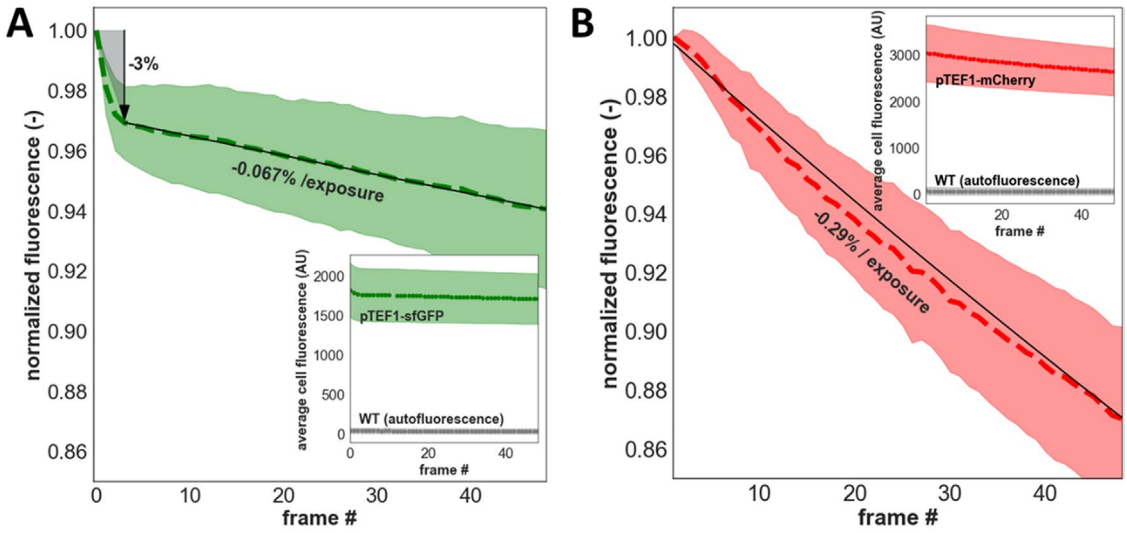

FIGURE 1: Determination of Whi5 concentration with wide-field fluorescence microscopy may be confounded by photobleaching. Photobleaching of sfGFP (A) and mCherry (B) expressed from the *TEF1* promoter. Cellular fluorescence was quantified as average fluorescence intensity within the cell mask and normalized to the value at the first time point. Cells were imaged over the course of 250 s for sfGFP and 270 s for mCherry to generate 49 images ("frames") with approximately 5 s between subsequent exposures. A change in fluorophore concentration due to protein synthesis, dilution, and degradation over the short time course of the experiment can therefore be neglected. Comparing fluorescence between wild-type cells and cells expressing the fluorophores from the *TEF1* promoter shows that cellular autofluorescence is negligible compared with the signal of the fluorescent proteins (inserts).

Plotting the data aligned for either birth (as done by Schmoller *et al.*, 2015) or for Start (as done by Litsios *et al.*, 2019) can indeed lead to different visual impressions (Supplemental Figure S1, A and B, respectively). Aligning the data for birth exaggerates the extremes and does not reflect the average population behavior. This is because the rightmost part of the average Whi5 concentration profile is dominated by the few cells that spend an unusually long time in G1 before Start. These cells grow more and thus show a larger apparent Whi5 dilution than most of the population. Because every cell passes Start at a different time point, in Litsios *et al.* (2019), we aligned the single-cell traces at Start, so that the average dilution of Whi5 at Start can be directly read off the plot (Supplemental Figure S1B).

However, it is important to note that to determine the Whi5 dilution factor from single-cell Whi5 data, one does not need to align the data at all. The dilution factor is a number that can be calculated for each cell using the Whi5 fluorescence intensity values and cell volume at birth and at Start, as shown in Supplemental Figure S1C. When calculating the Whi5 dilution factor using the integrated cell fluorescence divided by total cell volume as a proxy for protein concentration (as Schmoller *et al.*, 2015), various literature sources find the following values: Using Whi5-mCitrine, Schmoller *et al.* (2015) reported an average decrease in Whi5 concentration of 25% between birth and Start in daughters grown on synthetic complete (SC) medium with 2% glycerol and 1% ethanol as the carbon source (Figure 1G of Schmoller *et al.*, 2015), as measured in a *bck2*Δ strain that is partially defective for Start and 50% larger than the wild type. An average Whi5-mCherry decrease of 18% was observed for daughters grown in 2% glucose minimal medium (Figure 5A of Litsios *et al.*, 2019; Supplemental Figure S1B, C) using the same wide-field technique and concentration proxy as Schmoller *et al.* (2015). Decreases of similar magnitude (i.e., 12–25%) have also been reported in Qu *et al.* (2019) as well as in Litsios *et al.* (2019) for daughter cells grown on different carbon sources. Thus, using wide-field microscopy and the proxy of Schmoller *et al.* to estimate protein concentration consistently results in Whi5 dilution factors in the range of 12–25%.

As these are relatively small changes in apparent Whi5 concentration, it is critical 1) to assess any potential confounding effects arising from the use of time-lapse wide-field fluorescence microscopy and 2) to estimate the time dependence of Whi5 concentration with alternative experimental methods.

Variables affecting Whi5 concentration quantification by wide-field time-lapse fluorescence microscopy

Photobleaching is an inevitable confounding factor in time-lapse quantitative fluorescence microscopy (Cranfill *et al.*, 2016; Fadero *et al.*, 2018), and from our experience, it is extremely difficult, if not impossible, to fully avoid photobleaching when the same cells are imaged repeatedly over time. Here, we assessed to what extent our own published Whi5 experiments (i.e., Litsios *et al.*, 2019), obtained using wide-field fluorescence microscopy, were affected by photobleaching.

To quantitatively determine the extent to which bleaching can contribute to a decrease in Whi5 signal, we determined the bleaching rate of sfGFP and mCherry with imaging settings that closely resemble (for sfGFP) or are identical to (for mCherry) those that we used in Litsios *et al.* (2019), with which we had found 12% and 18% drops in Whi5 concentration, respectively. For these new photobleaching control experiments, we used strains that expressed the fluorescent proteins from a strong promoter (*TEF1*), such that the signal from the fluorescent protein was substantially greater than cellular autofluorescence (Figure 1, A and B, inserts) and hence the cellular autofluorescence can be neglected. To obtain the photobleaching curve, we then imaged 49 times the same cells (same fields of view [FOVs]) over ~4.5 min. Through this approach, which has been used in other studies to evaluate the rate of photobleaching (Fadero *et al.*, 2018), the acquired fluorescence data are only

minimally affected by synthesis of the fluorescent protein during the imaging period. The amount of light per exposure (i.e., light intensity times exposure duration) that we used for these bleaching tests was equal to (for mCherry) or very closely resembled (for sfGFP) the amount of light we used previously (Litsios *et al.*, 2019) to measure mCherry-Whi5 and Whi5-sfGFP. Specifically, for mCherry we used a light intensity of 50% (amounting to 5.1 nW/μm^2 measured at the specimen) and a 600 ms exposure and for sfGFP, 6% (9.8 nW/μm^2 measured at the specimen) and 100 ms. Even at this low-light intensity, we found that the fluorescence signal of sfGFP dropped by 3% over the course of the first four exposures and then subsequently by 0.067% with each additional exposure (Figure 1A) while each exposure reduced the mCherry fluorescent signal by 0.29% (Figure 1B).

While these bleaching rates appear low, with a G1 daughter length of 60 min and a 3-min sampling interval, the determined bleaching rate of mCherry would yield a signal drop of about 6% (i.e., [1-0.0029]^20 = 0.9435) in our wide-field microscopy experiments with Whi5-mCherry, assuming minimal synthesis of Whi5 during G1 (Litsios *et al.*, 2019). This photobleaching effect would thus account for approximately one third of the observed Whi5-mCherry signal decrease of 18% in our published data (Supplemental Figure S1B, C). With the more photostable sfGFP a lower drop in Whi5 signal would be expected, and consistently we previously found only an about 12% decrease in the signal of Whi5-sfGFP during G1 (Litsios *et al.*, 2019). These controls indicate that photobleaching occurs even with high-numerical-aperture objectives and low exposure settings and that it can contribute to an apparent decrease in Whi5 concentration observed with wide-field epifluorescence microscopy.

Another potential artifact connected with the determination of protein levels via wide-field microscopy can arise by the so-called "partial confocal effect" (Gordon *et al.*, 2007; Joglekar *et al.*, 2008; Verdaasdonk *et al.*, 2014). Light emerging from different depths of the specimen does not equally contribute to the overall signal that is measured at a pixel. In other words, while light coming from the focal plane is entirely detected and measured, slightly out-of-focus light is only partially accounted for. This effect, which has been observed for yeast cell imaging with high-numerical-aperture objectives (Gordon *et al.*, 2007; Joglekar *et al.*, 2008; Verdaasdonk *et al.*, 2014), could skew the concentration estimates as obtained by Schmoller and colleagues. Specifically, Schmoller and colleagues assume that the sum of pixel fluorescence intensities of a given cell is proportional to the *amount* of fluorescent protein in that cell. They then divide this sum by the cell volume to obtain a proxy for protein concentration. However, given the fact that the fraction of the fluorescence intensity attributable to out-of-focus light increases in larger cells (Gordon *et al.*, 2007), the concentration proxy used by Schmoller *et al.* (2015) could decrease as a cell grows during G1, even if the actual protein concentration stays constant. The contribution of this phenomenon to the quantification of large (e.g., severalfold) changes in protein concentration can be neglected but becomes potentially relevant for small changes in protein concentration such as those reported for Whi5. While we cannot quantitatively determine the degree of underestimation of the protein concentration due to this effect, when we alternatively use the average fluorescence intensity in a cell as another proxy of cellular protein concentration (a common practice in the field [Lo *et al.*, 2015], which we also implemented in Litsios *et al.* [2019] together with the concentration proxy approach of Schmoller *et al.*, 2015), then the fluorescence intensity drop of Whi5 during G1 is nearly zero (see WF-1 data in Figure 5A of Litsios *et al.*, 2019). Thus, partial confocal effects may also lead to an apparent drop in Whi5 concentration during G1, particularly for larger cells.

A third potentially confounding factor in the analysis of the Whi5-mCitrine time courses of Schmoller *et al.* (2015) (and our Whi5-mCherry and Whi5-sfGFP data shown in Figure 5A of Litsios *et al.*, 2019) lies in the fact that if Whi5 is indeed diluted during G1, then it must be the nuclear Whi5 that gets diluted because Whi5 resides mainly in the nucleus before Start. In this context, it is critical to note that neither Schmoller *et al.* (2015), nor the other authors of Schmoller *et al.* (2022), nor Litsios *et al.* (2019) measured the *nuclear* Whi5 concentration. Instead, all these authors divided the total

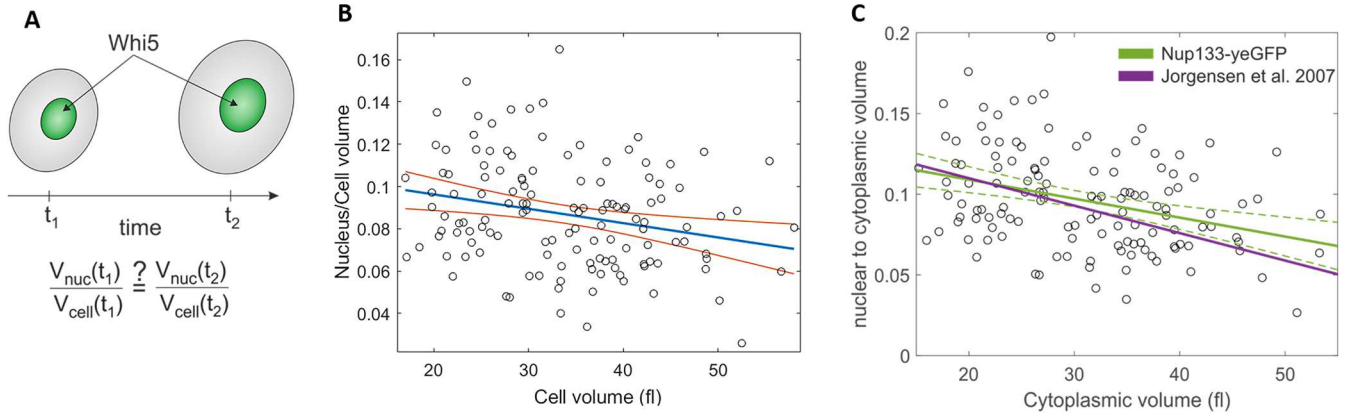

FIGURE 2: Determination of nuclear Whi5 concentration by wide-field fluorescence microscopy is confounded by nonproportional scaling of the nuclear-to-cell volume. (A) Schematic illustration of the nuclear-to-cell volume scaling problem. Whi5 is in the nucleus prior to Start. As time passes, cells grow, and so does the nucleus. Calculating nuclear Whi5 concentration by dividing total cell fluorescence by cell volume (as performed by Schmoller *et al.*, 2015) presupposes that the nucleus occupies a constant fraction of the whole-cell volume as cells grow during G1 phase. (B) Ratio of nuclear to whole-cell volume as a function of daughter cell volume. Nuclear volume was determined with Nup133-yeGFP, and cell volume was determined from bright-field images (see *Materials and Methods*). The regression line is shown in blue, and the confidence band for the regression line is shown in red. (C) Ratio of nuclear-to-cytoplasmic volume as a function of daughter cytoplasmic volume. The cytoplasmic volume was calculated as the difference between whole-cell and nuclear volumes. The regression line and confidence band for our data is shown in green. The respective regression line from Jorgensen *et al.* (2007) (purple), where this relationship between nuclear and cell volume during G1 was first reported, is reproduced for comparison.

Whi5 signal of a cell (which they interpret as the Whi5 amount, as discussed above) by the cell volume to obtain an estimate of Whi5 concentration. If the nuclear volume scales proportionally with cell volume during G1, then this approach could indeed be used to estimate the relative nuclear Whi5 concentration dynamics during G1, as illustrated in Figure 2A. However, it has been reported that although the nucleus of daughter cells grows during G1, it does not grow as fast as the cytoplasm (Jorgensen *et al.*, 2007). We confirmed this previous result using a strain with fluorescently tagged Nup133 (Nup133-yeGFP) to delineate the nuclear membrane and found that the average nucleus-to-whole-cell volume ratio decreases from around 10% in small daughter cells to around 7% in large daughters (Figure 2B). When the ratio of nuclear-to-cytoplasmic volume is plotted against cytoplasmic volume, as published previously (Jorgensen *et al.*, 2007), a highly similar regression line and negative correlation coefficient are obtained (Figure 2C), demonstrating that the nuclear-to-whole-cell volume ratio decreases through G1 phase.

To put the above numbers in perspective: given a cell volume increase of around 60% between birth and Start for a daughter cell in glucose medium (e.g., Figure 4 of Soifer and Barkai, 2014; Figure 3 of Litsios *et al.*, 2019), if Whi5 concentration is calculated by using cell volume as a proxy for nuclear volume, then the concentration of Whi5 would reveal a drop of around 10%, even if the nuclear protein concentration was assumed constant. This discrepancy becomes even larger if a cell grows more during G1. This means that an observed apparent Whi5 dilution of 18% based on the division of whole-cell fluorescence with cell volume, in reality corresponds to only a dilution of 8% for nuclear Whi5.

In summary, at least three effects can lead to an overestimation of the drop in Whi5 signal based on wide-field microscopy data. First, our photobleaching tests demonstrate that photobleaching can explain part of the dilution we observed with Whi5-mCherry, given the wide-field fluorescence imaging conditions used in our experiments. While we cannot comment on the imaging settings used previously (Schmoller *et al.*, 2015), these should not deviate much from the settings used here. Second, the partial confocal effect in combination with the method of Schmoller *et al.* to estimate intracellular protein concentration could lead to an underestimation of protein concentration, particularly as cell volume increases. Third, the incorrect assumption that the ratio of nuclear-to-cell volume remains constant during G1 leads to an overestimation of the decrease in Whi5 concentration in the nucleus. Together, these confounding effects could explain a large fraction of the modest apparent dilution of 12–25% observed by Litsios *et al.* (2019); Schmoller *et al.* (2015) and Qu *et al.* (2019), in a range of different growth conditions. Given these potential confounding effects, we believe that it is absolutely crucial to investigate Whi5 concentration changes during G1 with alternative experimental methods. In the following sections, we describe results from such orthogonal measurement approaches.

Assessment of Whi5 concentration by mass spectrometry does not reveal dilution

By mass spectrometric detection of Whi5 peptides, we did not observe any Whi5 dilution during G1 in cell cultures synchronized by elutriation (Litsios *et al.*, 2019). In their Letter, Schmoller *et al.* (2022) criticize two aspects of this mass spectrometry data set, namely 1) the potential for interference by foreign peptides from the rich growth medium used and 2) that signals of the measured unphosphorylated Whi5 peptides did not decrease as cells approach Start, which should happen due to CDK-dependent phosphorylation of Whi5 and concomitant signal loss of the unphosphorylated peptides. To demonstrate the validity of our original conclusion that Whi5 concentration does not decrease in G1, we performed additional mass spectrometry experiments. Specifically, we used elutriation to generate synchronized populations of cells grown on minimal synthetic medium, to avoid putative contamination from foreign peptides originating from YPD (yeast extract, bacto peptone, dextrose) medium. Synchronized cell populations obtained by elutriation were then subjected to mass spectrometric proteome analyses at 16 different time points. In this experiment, contrary to the protocol used in Litsios *et al.* (2019), we preserved protein phosphorylation by quenching cells with 10% trichloroacetic acid (TCA) directly after harvesting (Kanshin *et al.*, 2015).

Six Whi5 peptides were identified (Figure 3A), the signals of which were normalized to the summed signals of peptides of housekeeping proteins (Tdh3, Eno2, Act1) whose abundances reflect total protein content. The concentration of three Whi5 peptides (**SP**PTAAR, SEVFL**SPSP**R, NGFG**TPSP**P**SP**PGITK) declined (Figure 3B) until the budding index (Figure 3C) reached a value of ~0.5, at which point Start had occurred in most of the cells. These three peptides contain CDK phosphosites and are therefore expected to be phosphorylated as cells approach Start (Costanzo *et al.*, 2004; De Bruin *et al.*, 2004; Wagner *et al.*, 2009). As our mass spectrometry analysis detected only the unphosphorylated form of these peptides, the concentration of these forms should decrease over time, which is exactly what the data show (Figure 3B). As a control, the samples were treated with phosphatase to allow the entire pool of Whi5 peptides to be detected. In this test, we found that the concentration of two phosphatase-treated peptides (one with two documented phosphosites, SEVFLSPSPR, and as a control one without a phosphosite, LNYALVK) remained constant throughout G1 (Supplemental Figure S3), supporting the notion that the signal reduction for these peptides is due to increasing phosphorylation as cells approach Start, and contradicting Whi5 dilution. Furthermore, two other Whi5 peptides that do not bear CDK sites (LNYALVK, LQNGWTDK) and another peptide that contains a single CDK site (TLPELETELAPAVQ**TP**PR) remained unchanged over the entire 300 min observation period (Figure 3, D and E). It should be noted that the presence of the CDK consensus site on the latter peptide does not imply that it is phosphorylated as cells grow; our data suggest that the phosphorylation status of this peptide does not change during G1. Collectively, these new mass spectrometry results suggest that Whi5 concentration is constant during G1, consistent with the conclusion drawn previously (Litsios *et al.*, 2019).

Assessment of Whi5 concentration by scanning 2-photon microscopy reveals invariant Whi5 concentration in G1 cells

Time-lapse wide-field fluorescence microscopy is subject to photobleaching and partial confocal effects and furthermore cannot directly measure nuclear protein concentrations, as demonstrated above. Mass spectrometry, like immunoblot detection, is a population-level analysis method that also cannot resolve nuclear Whi5 concentration. Alternative experimental methods are therefore required to substantiate conclusions on nuclear Whi5 dynamics. Such alternatives are offered by microscopy methods that can directly measure nuclear Whi5 concentration.

In Dorsey *et al.* (2018), we used 2-photon (2p) scanning number and brightness (2psN&B) to show that nuclear Whi5 concentration is constant as a function of cell size during G1. In their Letter, Schmoller *et al.* (2022) stated that they are not familiar with 2psN&B and thus cannot judge the approach. 2psN&B is a well-established and widely used fluorescence fluctuation–based method for quantitative single-cell imaging (e.g., Nagy *et al.*, 2010; Hellriegel *et al.*, 2011; Moutin *et al.*, 2014; Bourges *et al.*, 2017; Cutrale *et al.*, 2019;

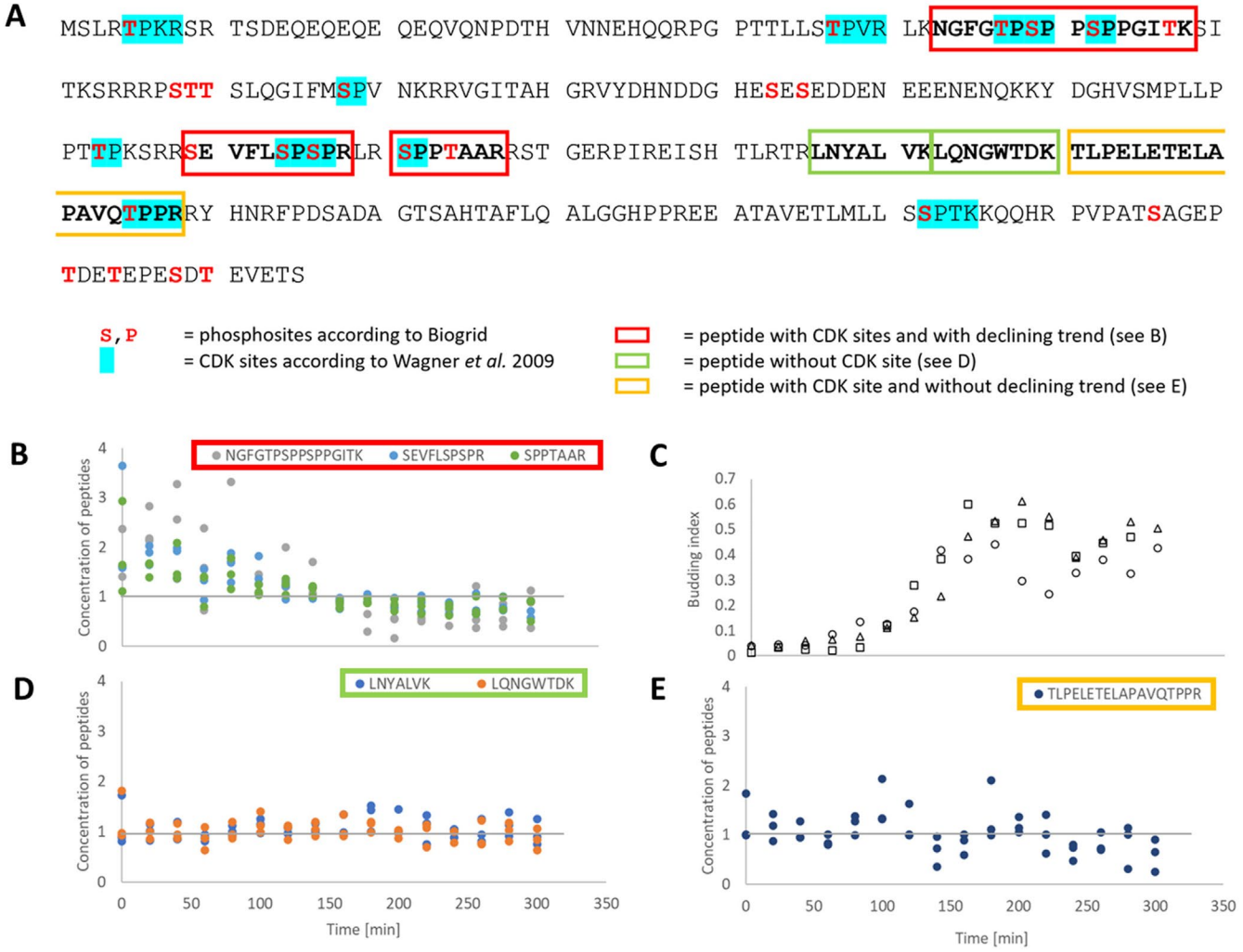

FIGURE 3: Mass spectrometry analysis demonstrates that Whi5 concentration is constant during G1. (A) Whi5 amino acid sequence; six peptides identified in our mass spectrometry analysis are indicated by colored boxes; red letters: known phosphosites according to BioGRID (https://thebiogrid.org/34481/protein); turquoise boxes: CDK sites according to Wagner *et al.* (2009). (B, D, E) Signals from six Whi5 peptides, normalized to the signals from housekeeping proteins (Tdh3, Eno2, Act1). The normalized values of a peptide from an experiment were then divided by the peptide's median value within this experiment. Data are from three independent cultivations, elutriations, and mass spectrometric analyses. Time point 0 indicates the moment when the elutriated cells were released into the fresh glucose minimal medium. Sampled cells were quenched with 10% TCA to prevent abiotic changes in protein phosphorylation. Note that the protein extraction protocol used in Litsios *et al.* (2019) was not explicitly designed to preserve protein phosphorylation such that any adventitiously dephosphorylated phosphopeptides would be expected to show a flat temporal behavior. (B) The signals of three Whi5 peptides that contain a CDK site and drop in signal. (D) The signals of two Whi5 peptides that do not contain any phosphosites. (E) The signal of a peptide with a single CDK site. An alternative normalization against all detected peptides in the proteome (instead of only those from the three housekeeping proteins) generated identical results (Supplemental Figure S2). (C) Budding indices as obtained in the three independent experiments.

Zamai *et al.*, 2019). 2psN&B can provide absolute protein concentrations, protein complex stoichiometry, and/or dynamic information on diffusion rates and has several advantages over wide-field fluorescence imaging. First, 2p imaging eliminates contributions from out-of-focus light because the 2p excitation volume is <1 fl and thus it is possible to gather light that emanates only from the yeast nucleus. Hence, 2psN&B is immune to partial confocal effects and nucleus-to-whole-cell volume ratio scaling effects. Second, because 2p microscopy excites in the infrared range (1000 nm), it diminishes the contribution of autofluorescence to the overall signal. Using this approach for GFP protein fusions at concentrations above 100 nM (such as nuclear Whi5-GFP), the contribution of autofluorescence is negligible (Dorsey *et al.*, 2018). Third, the lower excitation energy (1000 nm compared with 488 nm) causes less phototoxicity than visible light laser scanning confocal microscopy.

Using these advantages of 2psN&B microscopy, Dorsey *et al.* (2018) implemented an experimental approach that completely avoids photobleaching while determining nuclear Whi5 concentration during G1. Specifically, individual FOVs with cells of an asynchronously growing cell population were imaged only once and Whi5 concentration was then assessed as a function of size, not time. These results showed that the nuclear concentration of Whi5 was ~120 nM and that it remained constant with cell size in G1 phase (Figure 2 of Dorsey *et al.*, 2018). In the paper by Dorsey *et al.*, an

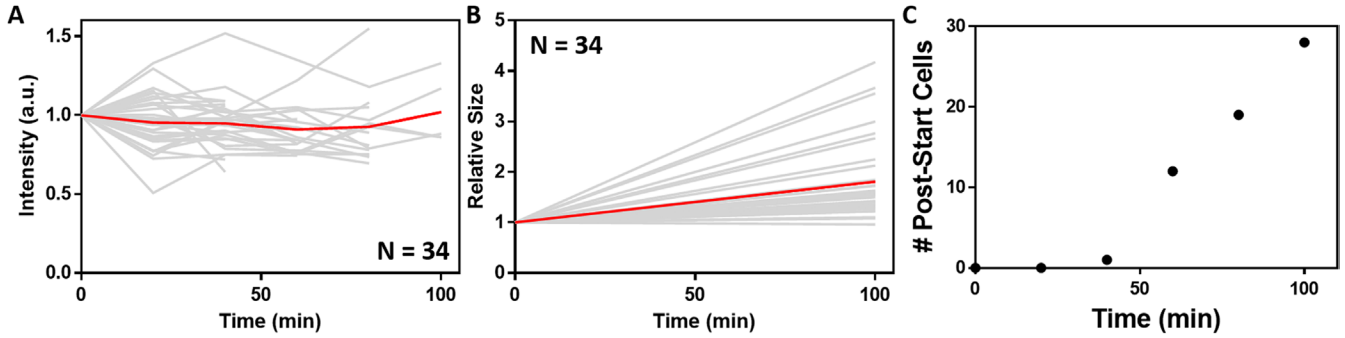

FIGURE 4: Nuclear Whi5-GFP intensity vs. time from repeated imaging of the same individual cells. (A) Whi5-GFP intensity relative to that obtained at time zero for 34 different cells (gray lines). Small daughter cells in an asynchronously growing population were chosen at the first time point and followed in successive images as a function of time. The average relative Whi5-GFP intensity for all 34 cells is plotted in red. Cells were followed until they passed Start (and Whi5 exited the nucleus), as discussed in the text. (B) Cell size was determined at two points: before the first Whi5-GFP time point and after the last Whi5-GFP time point from the masking of the entire cell images obtained from imaging at 750 nm. In gray are individual relative cell sizes, and in red is the average relative cell size for all 34 cells. A few of the cells had already passed Start at the end of the Whi5 imaging time course. The lines merely connect the initial and final size for each cell and do not represent growth curves per se. (C) Number of post-Start cells as a function of time (of the 34 daughter cells chosen at time point 1 and followed throughout the time course). Cells were counted as post-Start at the time point at which they exhibited no apparent nuclear Whi5-GFP localization.

additional approach where single cells were repeatedly imaged by 2psN&B as a time lapse series was also used to estimate changes in Whi5 concentration during G1. In this experiment, photobleaching was assessed by simultaneous imaging of a control strain expressing free GFP and was used to correct Whi5 concentration. We note that while Schmoller *et al.* (2022) criticize our time series analysis of a limited number of single cells, this experiment was only a confirmatory experiment for the main single-exposure 2psN&B results described above. This time-series control also demonstrated the importance of correction for photobleaching. The main conclusions of Dorsey *et al.* (2018) rest on the analysis of Whi5 concentrations as a function of cell size in hundreds of cells by a 2psN&B experiment that is immune to photobleaching. In their Letter, Schmoller *et al.* also criticize the differential absolute intensities in the single-image analysis experiment using 1p confocal microscopy published by Dorsey *et al.* (2018) (their Figure 3, G–J), where we imaged Whi5-GFP in thousands of cells from asynchronous populations in two different strain backgrounds (S288C, used in Dorsey *et al.*, 2018; W303, used in Schmoller *et al.*, 2015) on glucose and glycerol/ethanol medium. However, this criticism is not relevant because Schmoller *et al.* overlook the differences in autofluorescence between the two strains, which explain their differences in total signal intensity. A detailed analysis of autofluorescence in these strain backgrounds is provided in Supplemental Figure S4.

To further support the conclusion of Dorsey *et al.* (2018) that nuclear Whi5 concentration remains constant in individual cells during G1, we sought to perform time-dependent imaging of individual cells while mitigating photobleaching to the greatest extent possible. To this end, we repeatedly imaged asynchronously growing cells using 2p microscopy and analyzed the time-course data for small G1 daughter cells. We performed this experiment with our 2p system, where we further optimized the imaging parameters to minimize photobleaching: 1) 2p excitation laser intensity at 1000 nm for GFP detection was reduced to 30%; 2) a pixel dwell time of 64 µs was used to improve signal-to-noise ratio; 3) only five scans were acquired per time point and only at a single z-position; and 4) images were acquired only every 20 min (i.e., only six time points for the whole experiment). Using these imaging parameters, each pixel in the image was exposed to the exciting light for a total of less than 4 ms over the entire time course. We stress that because of point 3, we could not use the full fluctuation-based sN&B analysis procedure to extract the *absolute* Whi5 concentration; however, thanks to the advantages of the scanning 2p imaging system described above, we directly assessed the nuclear Whi5-GFP intensity free of the artifacts associated with wide-field imaging discussed above and used this nuclear Whi5-GFP intensity as a proxy for Whi5 nuclear concentration as a function of time/size in G1.

For accurate cell size assessment and to verify that cells grow normally under these conditions, we also acquired autofluorescence images in this experiment. To this end, we took advantage of the fact that 2p imaging allows separate excitation of autofluorescent molecules (λ_{ex} = 750 nm) and GFP molecules (λ_{ex} = 1000 nm). The autofluorescence images acquired only at the beginning and at the end of the Whi5-GFP imaging time course allowed us to detect the individual cell contours with high contrast and accuracy. This obviates the criticism by Schmoller *et al.* (2022) that the smallest cell sizes were underestimated in Dorsey *et al.* (2018), where the weak cytoplasmic Whi5-GFP signal was used to estimate size.

After completion of the imaging time course, the small daughter cells present at the first time point were indexed and their size was calculated by masking the autofluorescence images and counting the pixels within the masked region of each cell. Subsequently, the nuclei were masked in the Whi5-GFP images and the average intensity of the pixels within the individual nuclei was calculated. Here, we found that nuclear Whi5-GFP intensity in single cells remained constant as a function of time (Figure 4A), confirming that Whi5-GFP was not diluted as cells grew during G1 phase. The small daughter cells clearly grew over time (Figure 4B), and most (28/34) passed Start within 100 min (Figure 4C). These growth kinetics demonstrated that cells were not unduly stressed by the imaging conditions.

While the repeated-imaging approach described above can be used to follow Whi5 concentration over time, it is inherently low throughput and photobleaching cannot be fully excluded. On the other hand, while the assessment of Whi5 concentration as a function of cell size in asynchronous populations bypasses the photobleaching issue (as done in Dorsey *et al.*, 2018), it does not directly capture protein concentration as a function of time. To combine the

advantages of time-lapse imaging while eliminating any possibility of photobleaching, we additionally implemented a new approach in which a population of elutriated G1 cells was allowed to progress synchronously through G1 over time while residing on the microscope stage. Then, using 2p microscopy we imaged cells over different FOVs at each time point, such that each cell was illuminated only once during the 110 min duration of the experiment. We then determined the average nuclear Whi5-GFP intensity in the individual cells from these images and plotted these data as a function of time, which here corresponds to the progression through G1 of the synchronized population.

Analysis of these images demonstrated that the nuclear Whi5-GFP intensity was independent of the time elapsed after elutriation (Figure 5A, population 1; top bracket; averages shown in Figure 5B) and of the cell size in G1 cells (Figure 5C, population 1; top bracket). The slope for the linear fit of the population 1 data as a function of cell size (Figure 5D) was –0.004 ± 0.005 (R^2 = 0.004) and was not significant (p = 0.43). A second population of cells had no obvious nuclear localization of Whi5 (Figure 5, A and C; bottom bracket). These cells were evidently post-Start because Whi5-GFP had relocalized to the cytoplasm. The fraction of cells in this population increased as time elapsed after the elutriation (Figure 5E; Supplemental Figure S5); the imaged cells passed Start (as detected by loss of Whi5-GFP nuclear localization) with a midpoint at about 1 h (Figure 5E). Cells also grew over time, nearly doubling in size (Figure 5F; Supplemental Figure S5), indicating that they were not unduly stressed by the imaging conditions. The results of this experiment, which completely eliminates photobleaching, further substantiate the conclusion that no significant dilution of nuclear Whi5 occurs during G1 phase, despite cells undergoing a substantial increase in size.

Finally, for Whi5 concentration to remain constant as the cell grows during G1 phase, Whi5 must obviously be synthesized. Evidence for Whi5 synthesis in G1 phase comes from experiments in which the Whi5 concentration in G1 phase cells exceeds that predicted by volumetric dilution (Barber *et al.*, 2020) and by superresolution PALM microscopy experiments in which Whi5-mEos3.2 copy number scales with nuclear size (Black *et al.*, 2020). Further supporting Whi5 synthesis in G1, in a fluorescence recovery after photobleaching (FRAP) experiment we found that after complete bleaching of Whi5-mNeonGreen fluorescence in single cells, the nuclear intensity partially recovers as cells grow in G1 (Supplemental Figure S6; Supplemental Table 1).

In summary, wide-field microscopy time-course experiments yield a drop in Whi5 intensity over the course of the G1 phase of 12–25% when the Whi5 concentration is determined with the method of Schmoller *et al.* (2015). However, as we demonstrate here, this apparent decrease could be caused by photobleaching, by partial confocal effects, and by the assumption of a constant nuclear-to-cytoplasmic volume during G1. Orthogonal mass spectrometry approaches and microscopy techniques that avoid photobleaching and/or measure Whi5 directly in the nucleus reveal that there is no nuclear Whi5 dilution during G1.

CLN3 LEVELS PULSE PRIOR TO START

Averaging of single-cell time traces masks the Cln3 pulses prior to Start

We recently proposed that a burst in protein synthesis occurs in G1, which rapidly drives up the concentration of the highly unstable G1 cyclin Cln3, triggering Start (Litsios *et al.*, 2019). In their reanalysis of the published data from Litsios *et al.* (2019), Schmoller *et al.* averaged single-cell Cln3 concentration traces (obtained by dividing the Cln3 synthesis rate, which is proportional to Cln3 abundance, by the cell volume) aligned at budding on a real-time axis and drew conclusions from this single average curve. However, due to the pulsatile dynamics of Cln3 concentration and intrinsic cell-to-cell variability in G1 phase duration, this approach averages out the information present in the single-cell data generated in Litsios *et al.* (2019) (shown here in Figure 6A). The correlation between the Cln3 pulses and Start is visible in a heat map of the single-cell data (Figure 5B in Litsios *et al.*, 2019) replotted here on a real time axis (Figure 6B). Furthermore, while for most cells Start occurs after a single pulse of Cln3, in some cells a second pulse is required. Two Cln3 pulses occur mostly in cells with a long G1, likely because they failed to pass Start during the first pulse, as explained in Litsios *et al.* (2019). The Cln3 pulses are not random but are associated with other measured features (i.e., pulses in the rate of NAD(P)H change and the relocalization of Whi5 from the nucleus to the cytoplasm, which is only partial during the first pulse), as demonstrated (Figure 3F and Extended Data Figure 3D in Litsios *et al.*, 2019). As can be seen in the single-cell data shown in Figure 6C, the increase in Cln3 concentration is much larger than the 50% inferred by averaging the single-cell Cln3 signals (Figure 6C, red line). When accounting for the variability in G1 duration by averaging the single-cell Cln3 concentration traces on a normalized time axis, a 3.5-fold increase in the average Cln3 concentration is evident (Figure 4D in Litsios *et al.*, 2019). Thus, summarizing a variable single-cell data set by a single average value obscures the underlying single-cell dynamics and leads to incorrect conclusions with respect to the magnitude of Cln3 concentration changes.

Schmoller *et al.* criticize the analysis of single-cell time traces in Litsios *et al.* (2019) because 1) they believed that Cln3 abundance (i.e., total Cln3 signal) measurements were not converted into concentrations and 2) the fluorescence of the bud was not added to the fluorescence of the mother cell. First, Cln3 signals were in fact converted into concentrations in Litsios *et al.* (2019) (see their Figure 4D). Second, in all cases where protein synthesis rates were estimated for cell cycle phases in which the bud is present (i.e., Figures 2D and 4C in Litsios *et al.*, 2019), the total fluorescence intensity of both the mother and bud cell were included in the measurements. For the cases where only G1-specific protein production rates were of interest, mother cell fluorescence and volume were additionally measured for 18 min after bud appearance (identified by the appearance of a dark spot in the cell wall in bright-field images), in order to facilitate the smoothing of the trajectories around budding. In those cases, bud volume was not recorded because the volume of the growing bud at this stage is too small to be measured and represents only a tiny fraction of the mother volume. Truncation of the single-cell data at the moment of bud emergence demonstrates that the shape of the Cln3 concentration curves during G1 is not affected (Supplemental Figure S7). Thus, the criticism of Schmoller *et al.* on these aspects is not justified.

Mass spectrometry measurements reveal a clear Cln3 pulse prior to Start

Schmoller *et al.* raise the possibility that foreign peptides from the growth medium introduced artifacts in our Cln3 detection by mass spectrometry (Litsios *et al.*, 2019) and that putative noise from extraneous peptides invalidates our conclusions. Below, we demonstrate that the presence of foreign peptides does not bias our results and that our mass spectrometry data provide clear orthogonal evidence for Cln3 pulses prior to Start.

Because Cln3 is a low-abundance, extremely unstable protein, before our work Cln3 peptides had never been observed in any mass spectrometric analysis to our knowedge. To increase the chances of detecting Cln3 in our experiments, cells were grown in

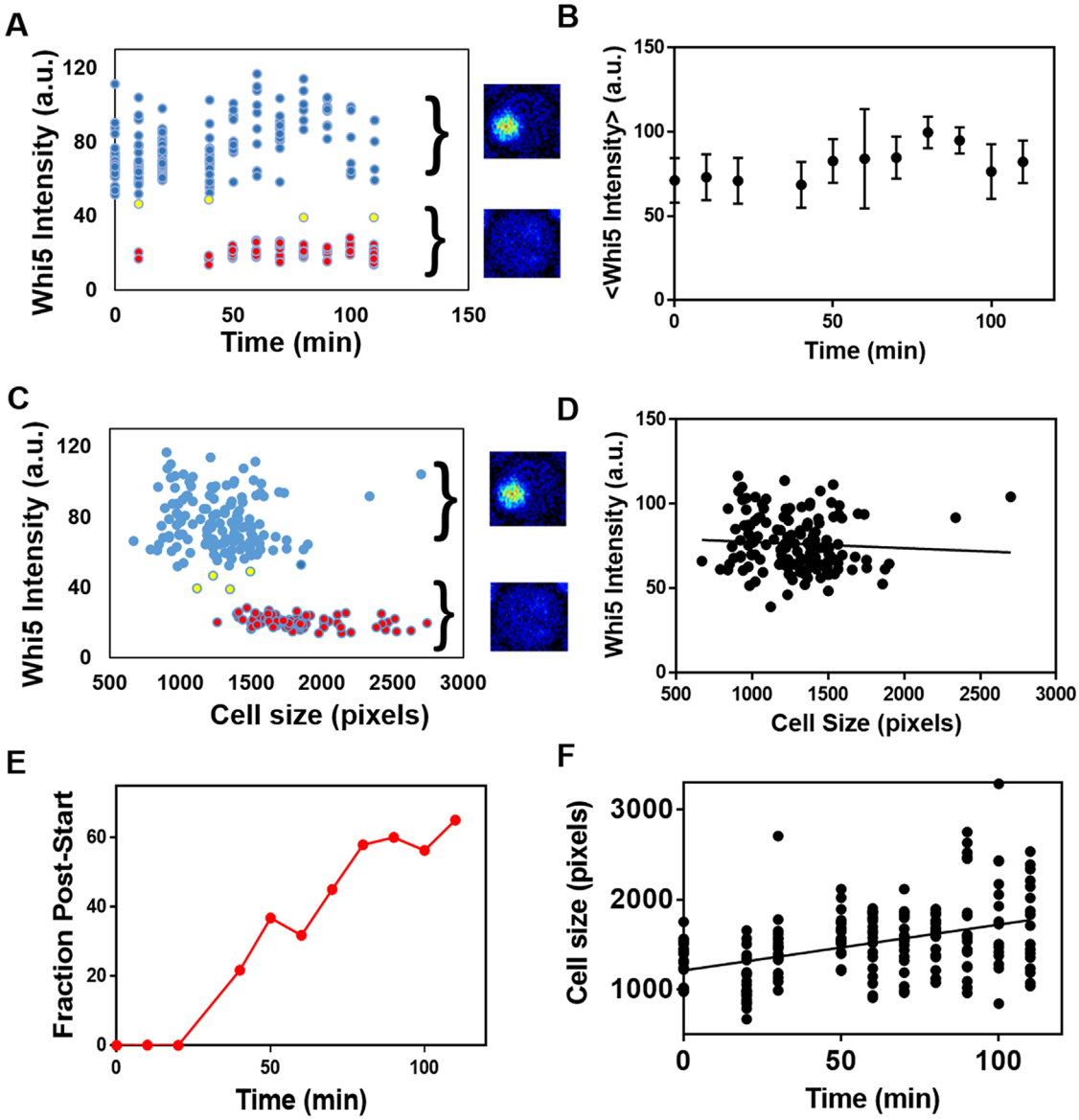

FIGURE 5: Whi5-GFP intensity vs. size and time in a synchronous G1 population. Different FOVs of elutriated Whi5-GFP cells in SC + 2% glucose were imaged at each time point. (A) Whi5 intensity vs. time. Blue dots indicate cells that had strong nuclear Whi5-GFP signal (termed population 1; see also Supplemental Figure S5) and had not passed Start, while red dots indicate cells that had no apparent nuclear Whi5-GFP localization (i.e., post-Start cells; termed population 2). A few yellow dots represent cells that were evidently in the process of transitioning through Start. (B) Average Whi5-GFP nuclear intensity of pre-Start cells as a function of time. (C) Whi5-GFP intensity as a function of size. In plots for either time (panel A) or size (panel C), there is a clear bimodal distribution of nuclear Whi5-GFP intensity (indicated by brackets) corresponding to pre-Start (high intensity, population 1) and post-Start (low intensity, population 2) cells, as shown by representative cellular images to the right of each graph. (D) Whi5 nuclear intensity vs. cell size for cells in population 1 (pre-Start). A linear fit yielded a slope of –0.004 ± 0.005, with a nonsignificant correlation coefficient, R^2, of 0.004; the p value for slope significantly <0 was 0.43. (E) Fraction of post-Start cells vs. time as indicated by lack of Whi5 nuclear localization. (F) Cell size vs. time. The linear fit yielded a slope of 5.1 ± 0.8, a correlation coefficient, R^2, of 0.176, and the p value for slope significantly >0 was <0.0001. The individual cell intensity values correspond to the brightest of the three z-positions imaged in order to obtain the best focus on individual nuclei (Supplemental Figure S5). Of the 231 cells imaged, only three or four (<2%) (yellow in A and C) exhibited intermediate Whi5-GFP intensities. These cells were likely caught in the act of passing Start. The excitation wavelength was 1000 nm. Images were averages of five scans with 40 µs pixel dwell time.

rich medium (YPD) to maximize the protein synthesis rate. In addition, cell pellets were not washed after removal of growth medium because any washing step could have resulted in Cln3 degradation before freezing the samples (Kanshin *et al.*, 2015). These considerations meant that interfering yeast peptides might in principle originate from the small amount of residual YPD medium, although such effects have never been observed as far as we are aware. To test for potential interfering yeast peptides from the medium, we carried out a tryptic digest and mass spectrometric analysis on pure YPD medium (Supplemental Figure S8). Here, only ~100 peptides could

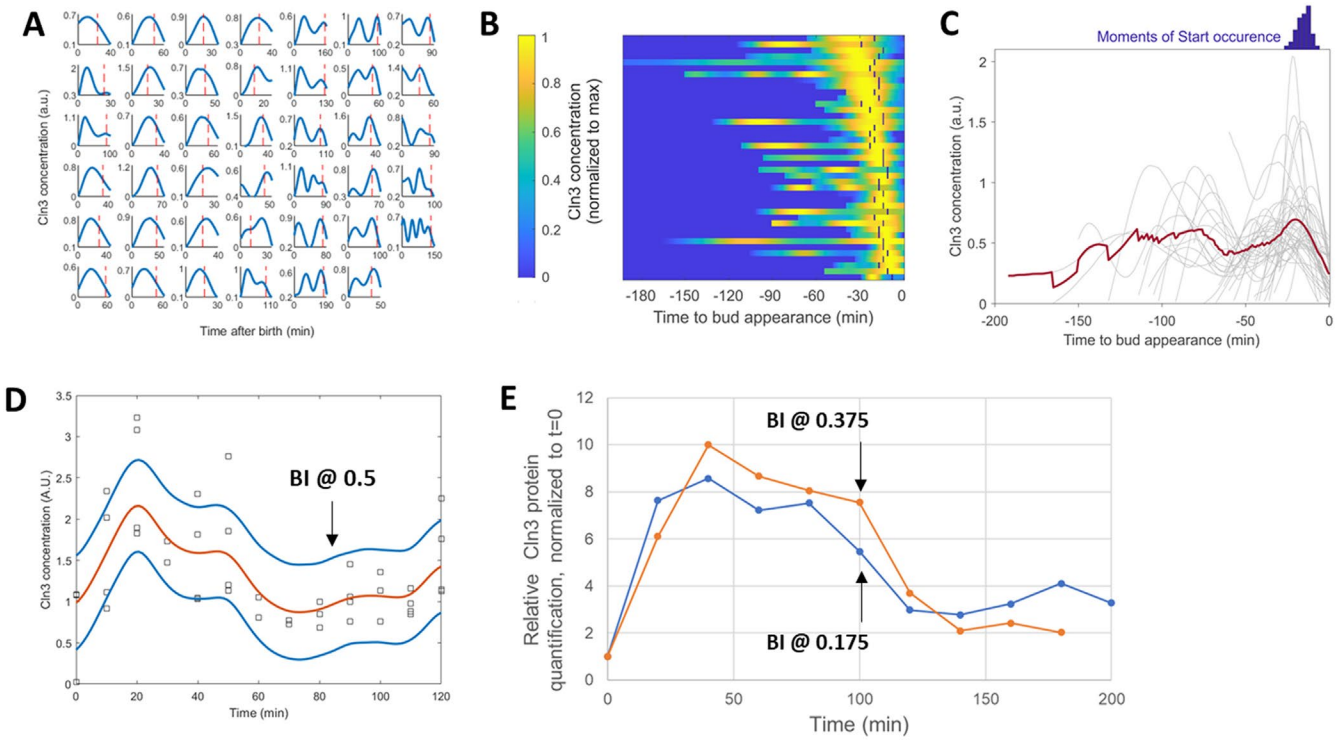

FIGURE 6: Cln3 levels pulse prior to Start. (A) Single-cell traces of Cln3 concentration in daughter cells during G1 (i.e., from birth up to bud appearance). For each cell, we first estimated the abundance of Cln3 over time using Gaussian process regression (cf. with Litsios *et al.*, 2019) and then divided this abundance by the cell volume. The vertical lines indicate the complete exit of Whi5 from the nucleus as a marker of Start. (B) The same data as in A, presented as a heatmap, where the color scheme represents the Cln3 concentration. For each cell, the Cln3 concentration time series was divided by the maximum value attained during the corresponding observation window. The dark rectangles indicate the moment of Start in each cell. (C) The same data as in A aligned for budding. Here, clearly one (or two) peaks are visible. The small histogram shows the distribution of times when Start happened in the monitored cells. The red line corresponds to the average, which is what Schmoller *et al.* (2022) plot in their Letter (their Supplemental Figure S8). As can be seen, this average cannot capture the true range of Cln3 dynamics. (D) Cln3 concentrations determined by mass spectrometry from four independent elutriation and analysis runs for cells grown on YPD; data are from Litsios *et al.* (2019). Uncertainty is estimated with Gaussian process regression. The orange line denotes the posterior mean function (smoothed estimate of the data), and the blue lines denote the band of 70% posterior confidence. The time at which budded cells reached 50% of the population (BI@0.5) is indicated. (E) Western blot data published in Lucena *et al.* (2018) for an elutriated cell population. Cln3 abundance is relative to a loading control. Data normalized at $t = 0$. Original data were obtained from Lucena *et al.*, including an additional unpublished replicate experiment; red and blue lines indicate the two experiments. The times at which budded cells reached 17.5% and 37.5% of the population (BI@0.175, BI@0.375) are indicated.

be detected in total compared with 9,000 total peptides in our published experiments, and none of these peptides was derived from Whi5 or Cln3. This demonstrates that our previously reported measurements were not confounded by medium-derived peptides. By combining the signals from the two measured Cln3 peptides, which as demonstrated stem from the yeast cells, across four independent elutriation time courses and estimating the uncertainty in the data with Gaussian process regression, we observe a clear increase in Cln3 concentration prior to Start followed by a decline (Figure 6D), supporting our published conclusion that Cln3 pulses occur prior to Start (Figure 4D from Litsios *et al.*, 2019).

Cln3 oscillations have been documented in the recent literature

In their Letter, Schmoller *et al.* also counter the evidence for a Cln3 pulse prior to Start based on their reanalysis of previously published Western blot experiments on synchronous cell populations obtained by elutriation (Lucena *et al.*, 2018). We have reservations about the Western blot quantification in the reanalysis of this data by Schmoller *et al.* (i.e., their Supplemental Figure S4D, E). First, the concentration of the stable Whi5 protein appears to drop by 300% despite an increase of only 60% in cell volume. Second, only the first 100 min of the elutriation time course are plotted. Plotting the Cln3 concentration over the full time course reveals a clear pulse of Cln3 (Figure 6E). This Cln3 pulse is consistent with earlier elutriation-Western blot experiments (Thorburn *et al.*, 2013; Zapata *et al.*, 2014), with recent new experiments (Sommer *et al.*, 2021), and with our published findings (Litsios *et al.*, 2019).

GLOBAL PROTEIN SYNTHESIS RATES INCREASE PRIOR TO START

Finally, we observed a two- to threefold increase in the global protein synthesis rate prior to Start (Litsios *et al.*, 2019) based on the accumulation of stable sfGFP driven by the constitutive *TEF1* promoter. On the basis of their own data from another stable protein (mCitrine) whose expression was driven by the *ACT1* promoter, Schmoller *et al.* (2022) state that they did not find any evidence for an increase in the global protein synthesis rate. Our reanalysis of the

Schmoller *et al.* data, however, reveals that, in fact, the protein synthesis rate monitored by the *ACT1*-mCitrine reporter does increase in G1. Even from the average of single-cell mCitrine abundance time traces in the Letter of Schmoller *et al.* (aligned at budding; Figure 3A of their Letter and reproduced here in Supplemental Figure S9) it can be readily seen that mCitrine accumulates slowly during early G1 (–100 to –60 min before budding) but then the rate of accumulation increases considerably as cells approach Start in late G1. Linear regression of these two phases of the digitized data from Figure 3A (Schmoller *et al.*, 2022) reveals that the protein synthesis rate is more than threefold faster in late G1 compared with early G1 (slope of first phase: 4.58; slope of second phase: 15.9) (Supplemental Figure S9). This reanalysis supports our conclusion that an increase in the global protein synthesis rate occurs in late G1 prior to Start. Furthermore, consistent with the global proteins synthesis dynamics we reported in Litsios *et al.* (2019), recent work shows that protein synthesis occurs predominantly in G1 and decreases thereafter (Campbell *et al.*, 2020).

CONCLUSION

In this Response, we have provided additional experimental evidence and analyses demonstrating that our previous conclusions on Whi5, Cln3, and protein synthesis dynamics (Dorsey *et al.*, 2018; Litsios *et al.*, 2019) are robust. As the present study shows, for any biological phenomenon purported to derive from modest time-dependent changes in protein concentration, extreme care must be exercised to account for experimental factors that lead to potential signal loss. Our previous studies (Dorsey *et al.*, 2018; Litsios *et al.*, 2019; Black *et al.*, 2020) and the additional experiments reported here provide a coherent body of evidence that Whi5 is not diluted by measurable amounts during G1 phase, hence making less likely the hypothesis that Start is primarily triggered by Whi5 dilution. Results inconsistent with the Whi5 dilution model of Start control during G1 phase have also been reported elsewhere (Blank *et al.*, 2018; Garmendia-Torres *et al.*, 2018; Barber *et al.*, 2020; Sommer *et al.*, 2021). In addition to evidence from our groups, other previous work also suggests that Start is controlled primarily by the increase in the protein synthesis rate in G1 phase and the concomitant synthesis of the unstable Start activator Cln3 (Thorburn *et al.*, 2013; Zapata *et al.*, 2014; Sommer *et al.*, 2021). We emphasize that while Cln3 is a primary activator of Start, the commitment decision undoubtedly depends on multiple different inputs (Chen *et al.*, 2020), including the accumulation of SBF subunits (Harris *et al.*, 2013; Dorsey *et al.*, 2018), titration of G1/S promoters (Wang *et al.*, 2009), additional signaling events (Talarek *et al.*, 2017), metabolic status (Litsios *et al.*, 2019), and other as-yet-undeciphered genetic determinants (Jorgensen *et al.*, 2002; Zhang *et al.*, 2002; Soifer and Barkai, 2014). While we do not dispute that dilution of Whi5 or any other repressor is one theoretical mechanism that could help cells sense growth, we do not find evidence for Whi5 dilution in the experimental contexts we have tested.

Data availability

Figure 1: https://doi.org/10.34894/SWRBYR

Figure 2: https://doi.org/10.34894/TFC012

Figure 3: https://doi.org/10.6019/PXD029959

Figure 4: https://doi.org/10.34894/IVWACK

Figure 5: https://doi.org/10.34894/HNWBYM

Figure 6: https://doi.org/10.34894/PKZZOJ

MATERIALS AND METHODS

Yeast strains and growth media

Strain backgrounds used were the prototrophic *Saccharomyces cerevisiae* strain YSBN6 (*MAT***a**; genotype: FY3 ho::HphMX4 derived from the S288C strain background [Winston *et al.*, 1995]), the BY4741 derivative of S288C, and W303. Standard yeast medium formulations were used as detailed for each type of experiment below.

Quantification of photobleaching rates

Light intensity at the specimen was measured using a Thorlabs S121C light sensor (400–1100 nm, 500 mW). First, to determine the area of the objective from which light was emitted during these measurements, a wild-type *S. cerevisiae* cell suspension in demineralized water containing trace amounts of the green fluorophore 5(6)-carboxy-2′,7′-dichlorofluorescein was prepared and loaded on a microscopy slide. While live imaging in the GFP channel, the focal plane was chosen by focusing on the yeast cells. The fluorescent dye provided contrast to clearly show the opening of the manually operated pinhole of the microscope. This pinhole was closed to such an extent that a hexagon was visible inside the FOV. The area of this hexagon was determined by masking it by hand using NIS Elements AR software (Nikon). Next, the light was switched to the wavelength and intensity we wanted to measure. The light sensor was set to low-bandwidth measurement and was held over the objective at the specimen location. The optimal sensor position was determined by reading the live output of the sensor and recording the maximum power (in μW) measured. Finally, this power was divided by the aforementioned pinhole area from which the light was emitted, yielding the light intensity in nW/μm^2. The light intensity of the GFP excitation light was measured at 470 nm while the intensity of the RFP excitation light was measured at 565 nm.

For the bleaching experiments, we used *S. cerevisiae* YSBN6 expressing sfGFP or mCherry from the pTEF1 promoter, mixed with wild-type cells at a ratio of 4:1. Cells were placed under an agar slab and were imaged with a 5 s gap between exposures. For pTEF1-mCherry, we used 50% light intensity and a 600 ms exposure. For pTEF1-sfGFP, we used 6% light intensity and a 100 ms exposure. The imaging interval was corrected for the actual exposure time, that is, 5.6 s for pTEF1-mCherry and 5.1 s for pTEF1-sfGFP. To obtain 49 frames for either fluorophore, the total experiment duration was 4 min 30 s for RFP autofluorescence/pTEF1-mCherry and 4 min 10 s for pTEF1-sfGFP/GFP autofluorescence. Each position was imaged in bright field before and after completion of the bleaching experiment.

Fluorescence images were background corrected using a 50 pixel rolling ball algorithm. Cell masks were obtained by applying the ImageJ plug-in BudJ (Ferrezuelo *et al.*, 2012) on bright-field images. For the bleaching experiments, cell segmentation was performed on the bright-field image obtained after each experiment. The cell masks were applied to the background-corrected fluorescence images so that average cellular fluorescence could be calculated. Small cells (with a volume ≤20 fl) were excluded from analysis because their relative growth over the experiment might be nonnegligible.

We normalized the average cell fluorescence of individual cells to the value recorded in the first frame. Then, to determine the exponent of the fitted decay function, we took the natural logarithm of the population-averaged normalized fluorescence and determined its slope and offset. For mCherry, all data were used because the decay rate is constant. For sfGFP, on the other hand, the first three data points were not used because the constant exponential decay set in only after the third exposure.

All images were acquired on Nikon Eclipse Ti-E inverted wide-field fluorescence microscopes fitted with the Nikon Perfect Focus System (PFS) to maintain focus during time-lapse movies and Andor iXon Ultra 897 DU-897-U-CD0-#EX cameras. For fluorescence images, the readout mode was set to 1 MHz at 16 bit with an EM gain factor of 25. For bright-field images, excitation came from a halogen lamp fitted with a 420 nm beam splitter and the readout was performed at 1 MHz and 16 bit without gain amplification. To image Whi5-mCherry and autofluorescence in the RFP channel, we used a 100× Plan Apo VC Oil objective (NA 1.40; Nikon), excitation at 565 nm from a CooLED pE-2 excitation system, a 560/40 nm band-pass filter, a 585 nm beam splitter, and a 630/75 nm emission filter. Autofluorescence in the GFP channel and Whi5-sfGFP were imaged using a 100× S Fluor Oil objective (NA 1.30; Nikon), a Lumencor AURA excitation system to excite at 485 nm, a 470/40 nm band-pass filter, a 495 nm beam splitter, and a 525/50 nm emission filter. The temperature of the specimen was kept constant at 30°C using a microscope incubator box (Life Imaging Services).

Nuclear volume determination

Wide-field microscopy experiments were performed using an inverted fluorescence microscope (Eclipse Ti-E; Nikon Instruments). Temperature was kept constant at 30°C using a microscope incubator (Life Imaging Services). A 100× Nikon S Fluor (N.A. = 1.30) objective was used. Images were recorded using an iXon Ultra 897 DU-897-U-CD0-#EX camera (Andor Technology). Fluorescence measurements were performed using an LED-based excitation system (Lumencor; AURA). For GFP measurements, cells were excited at 470 nm (excitation filter: 450–490 nm, dichroic: 495 nm, emission filter: 500–550 nm). During bright-field imaging a long-pass (600 nm) filter was used. The Nikon PFS was used to prevent loss of focus.

For the determination of the nucleus-to-cell volume ratio across daughter cells of different sizes, we imaged daughter cells at the moment of birth and at budding. Cells expressing Nup133-yeGFP were grown in synthetic complete (SC) medium with 2% glucose, placed under a prewarmed agar pad (synthetic complete medium + 2% glucose + 1% agarose) and imaged for several hours. Multiple, nonoverlapping *XY* positions were recorded, and for each position bright-field and GFP fluorescence images were obtained every 5 min.

Fluorescence channel images were background corrected using the rolling ball background subtraction plug-in in ImageJ. For daughter cells the moment of birth was identified by the darkening of the bud neck while the moment of budding was identified by the appearance of a dark spot on the cell wall. Cells were first segmented using the semiautomated ImageJ plug-in BudJ (Ferrezuelo *et al.*, 2012), and the cell volume output from BudJ was used for subsequent analysis. For the segmentation of the nucleus the background-corrected fluorescence images were subsequently analyzed using a custom-made Python script and the segmentation boundaries detected by BudJ. First, for each cell, an intensity threshold was applied in the fluorescence channel inside the boundaries detected by BudJ; the generated mask was subsequently cleaned by applying several morphological operations (hole filling, dilation, and erosion). The boundaries of the mask were detected by using the *findContours* function from the *OpenCV* library in Python (Bradski, 2000), and an ellipse was fitted to the boundaries by using the function *fitEllipse* from *OpenCV*. The volume of the nucleus was calculated assuming the segmented ellipse as the middle section of an ellipsoid with the third radius equal to the semiminor axis of the segmented ellipse.

2-photon imaging

For all 2p imaging, Whi5-GFP was imaged exciting at 1000 nm, while autofluorescence was imaged exciting at 750 nm. Emission for both was obtained in the green channel (530 ± 50 nm band-pass filter). Autofluorescence images were masked by thresholding the counts outside cells and using our MATLAB scripts for edge detection. Cell size was calculated as the number of pixels within the cell outlines obtained from the autofluorescence masking. To calculate the average nuclear Whi5 intensity, nuclei were masked using a threshold to remove cytoplasmic intensity and the same edge detection techniques. The intensities for all pixels within each nucleus were summed and divided by the total number of pixels to obtain the average nuclear intensity. Cell indices were matched manually between the autofluorescence and Whi5-GFP images.

Cell size distributions were measured on a Beckman-Coulter Z2 multisizer. For steady-state asynchronous population imaging, cells from a single colony were grown overnight in 1 ml of SC 2% glucose medium until saturation. A small volume of this preculture was used to inoculate 1 ml of fresh SC + 2% glucose medium and allowed to grow to exponential phase (OD_{600} of 0.16–0.18, cell density 1–2 × 10^6 cells/ml). Two hundred microliters of the log-phase culture was pelleted in a microfuge at 1300–1500 rpm for 30 s and 195 µl of supernatant discarded. Cells were immediately resuspended in the remaining 5 µl and then 3 µl of the suspension placed on an agarose pad (62 µl) to a final cell density of ~2–3 × 10^6 cells/ml. Images were taken at 256 × 256 pixels in a 20 µm × 20 µm area. For the time course on the same cells, asynchronously growing cells were grown to log phase and placed on agarose pads as above at the same density.

For the time-course experiments on different FOVs, G1 cells were obtained using centrifugal elutriation. Cells were grown in 1 l of SC + 2% glucose overnight and centrifuged in a Sorvall SLC-6000 rotor at 1100 rpm for 10 min at 4°C. Cells were collected and lightly sonicated (30 s, 1 s intervals at power level 1) and elutriated at 1500 rpm using the supernatant as the sample medium. Cells were loaded into the elutriator at 8 ml/min and eluted at 12 ml/min. Fractions with cell size peak <20 fl (fraction number 2), as measured by a Beckman-Coulter multisizer, were used for subsequent time-series image analysis of nonoverlapping FOVs.

Whi5-GFP intensity versus size and time on different FOVs of elutriated wild-type Whi5-GFPmut3 cells (referred to as Whi5-GFP, derived from the BY4741 [S288C] strain background) grown in SC + 2% glucose was obtained from 2p images for each time point. The excitation wavelength was 1000 nm at 35% input power. Images (256 × 256 pixels in 20 µm × 20 µm) were averages of five scans with 40 µs pixel dwell time. The reported individual nuclear intensity values correspond to the highest average value for all nuclear pixels in each cell of the three z-scan positions (0 and ± 500 µm) imaged in order to obtain the best focus on individual nuclei (Supplemental Figure S5). Autofluorescence was imaged for each FOV at each time point at a single z-position with only three scans acquired also at 40 µs pixel dwell time.

To minimize photobleaching in time courses of the same FOVs, 2p excitation intensity at 1000 nm was reduced to 30%, and scans were acquired at a single z-position per time point with a slightly longer pixel dwell time of 64 µs to maximize the signal-to-noise (S/N) ratio. Furthermore, images were acquired only every 20 min (six time points only). Autofluorescence images used for accurate size assessment (excitation at 750 nm) were acquired only twice, once before the first Whi5-GFP time point acquisition and once after the last time point at a single Z position at 30% power also with a 64 µs pixel dwell time.

Whi5 FRAP-FLIM measurements

Wild-type cells expressing a Whi5-mNeonGreen (Whi5-mNG) construct from the *WHI5* endogenous promoter (Dorsey *et al.*, 2018) (derived from BY4741, S288C strain background) were grown to saturation overnight in SC + 2% glucose medium at 30°C in a rotary incubator and then diluted 100-fold in fresh SC + 2% glucose medium 6 h before imaging. The resulting asynchronous Whi5-mNG cultures were prepared for imaging on agarose pads as described (Dorsey *et al.*, 2018) and in the preceding section (*2-photon imaging*). The culture growth medium was reused to make the imaging pads in order to prevent nutrient up- or downshifts. For this purpose, 1 ml of cell culture was pelleted at 15,000 rpm for 1 min and 500 µl of the cell-free supernatant was mixed with 10 mg of agarose and warmed for 1–2 min at 98°C to melt the agar, followed by deposition of 62 µl on a coverslip to make the agarose pad. Cells were added after 20 min of pad cooling. Samples were imaged on an ISS Alba system composed of an inverted confocal Nikon Eclipse microscope equipped with a 100× water objective, a Fianium Whitelase continuous white laser with 488 nm emission filters, and single-photon APD detectors. Imaging was performed in time-domain fluorescence lifetime imaging mode (TD-FLIM [Lakowicz *et al.*, 1992]), whereby photons were collected over three raster scans of the same 30-µm-wide FOVs of 256 pixels (pixel size 117 nm), using an excitation power of 1–2 µW at 488 nm wavelength (20 MHz pulse frequency) and a 64 µs pixel dwell time.

G1 cells showing a prominently nuclear Whi5 localization were photobleached sequentially using a single-point FCS acquisition of 30 s, which was sufficient to completely suppress both mNG and autofluorescence signals. The z-focus was adjusted every 4–5 cells. Postbleaching control images were acquired after 20 min, followed by recovery for 60 min, and the same FOVs were imaged again in TD-FLIM mode.

The fluorescence lifetime was analyzed using the ISS Vistavision software. For each FOV separately, the fluorescence decay curve was constructed by accumulating Whi5-mNG photons from all G1 cells before photobleaching and after 60 min of recovery. Bins (n = 256) covering the 50 ns time interval between consecutive laser pulses were used to define the decay curves. Decay curves could be well fitted with a single-component exponential decay, from which the FOV-averaged lifetime was extracted. This single exponential decay was inconsistent with autofluorescence (Bhatta *et al.*, 2006; Maltas *et al.*, 2015). Cells expressing monomeric mNG from the inducible *GAL1* promoter (pGAL1-mNG) were used as a control for mNG fluorescence lifetime.

Measurement of Whi5 peptides by mass spectrometry in cell-cycle–synchronous cultures

For the proteomics experiments, single colonies of a YSBN6 Whi5-mCherry Hta2-sfGFP strain (Litsios *et al.*, 2019) were used to inoculate minimal medium (Verduyn *et al.*, 1992) with 20 g/l glucose. After overnight growth, cultures were diluted in fresh media and, when at OD_{600} 2, used to inoculate a 1.5 l bioreactor. The OD_{600} in the bioreactor was then kept at 2 using a custom-build turbidostat device. Elutriation was performed similarly as described previously (Rosebrock, 2017). For each elutriation run, 1 l of turbidostat culture was loaded into a large elutriation chamber (40 ml) at a pump speed of 40 ml/min and rotor speed of 3200 rpm. The elutriation buffer was minimal medium prewarmed at 30°C, with glucose and ethanol concentration adjusted to reflect their concentration in the flask culture at OD 2 (16 and 1.4 g/l, respectively). Approximately 300 ml of media containing small-sized cells were collected by increasing the pump speed to 68 ml/min. The elutriated cells were immediately incubated at 30°C with shaking. Sampling took place every 20 min. A volume between 9 and 35 ml was mixed with ice-cold 100% TCA to a final TCA concentration of 10% and centrifuged (5 min; 3200 × g) and the pellet was washed twice with ice-cold phosphate-buffered saline and flash-frozen in liquid nitrogen. At each time point, 100 µl of culture was also used to measure the cell size distribution of the population using CASY TT and 200 µl of culture was fixed with 4% formaldehyde for determining the budding index via microscopy.

Cell pellets were reconstituted in 400 µl 8 M urea, 50 mM Tris-HCl, pH 8, and bead beaten for 10 min at 30 Hz with a Retsch MM400. Cysteines were reduced for 1 h at 37°C in 5 mM TCEP. The protein concentration was determined by BCA assay (Thermo; 23252). Alkylation was performed by the addition of iodoacetamide to a final concentration of 40 mM and incubation for 30 min in the dark at 25°C. Samples were diluted 1:5 using 50 mM Tris-HCl and mass spectrometry–grade trypsin (Promega; V5280) was added at a ratio of 1:50 (µg trypsin: µg protein) and incubated overnight at 37°C at 400 rpm. The reaction was stopped by adding trifluoroacetic acid (TFA) to a final concentration of 1%. Sample cleanup by solid phase extraction was performed with Strata C18-E 50 mg/1 ml columns on a CHROMABOND vacuum stand, as follows. Columns were first conditioned with 50% acetonitrile (ACN) and equilibrated with 0.1% TFA. Each peptide sample was loaded, washed twice with 5% ACN, 0.1% TFA, and eluted with 50% ACN, 0.1% TFA. The eluate fraction was dried under vacuum and reconstituted with 0.1% formic acid at a peptide concentration of 0.5 µg/µl.

For enzymatic peptide dephosphorylation, sample aliquots containing a total of 10 µg of desalted peptides were dissolved in 50 µl of reaction buffer (50 mM HEPES, 100 mM NaCl, 1 mM $MnCl_2$, 1 mM $MgCl_2$, pH 7.4), and 2000 U of Lambda Protein Phosphatase (Lambda PP) and 20 U of Alkaline Phosphatase Calf Intestinal (CIP, both from New England BioLabs) were added and the sample was shaken at 600 rpm and 30°C for 1 h, as recently described (Dreier *et al.*, 2018). Peptide samples were cleaned up by solid-phase extraction as before, dried under vacuum, and reconstituted with 0.1% formic acid at a peptide concentration of 0.5 µg/µl.

For the targeted PRM-LC-MS analysis of the Whi5 protein, in a first step, parallel reaction-monitoring (PRM) assays (Peterson *et al.*, 2012) were generated from a mixture containing 500 fmol of each heavy reference peptide (JPT Peptide Technologies GmbH), iRT KIT peptides according to the manufacturer's protocol (Biognosys, Schlieren, Switzerland), and shotgun data-dependent acquisition (DDA) LC-MS/MS analysis on a Q-Exactive HF platform. The setup of the µRPLC-MS system was as described previously (Ahrné *et al.*, 2016). Chromatographic separation of peptides was carried out using an EASY nano-LC 1000 system (Thermo Fisher Scientific), equipped with a heated RP-HPLC column (75 µm × 30 cm) packed in-house with 1.9 µm C18 resin (Reprosil-AQ Pur; Dr. Maisch). Peptides were analyzed per LC-MS/MS run using a linear gradient ranging from 95% solvent A (0.1% formic acid in water [vol/vol]) and 5% solvent B (80% ACN, 19.9% water, 0.1% formic acid [vol/vol/vol]) to 45% solvent B over 60 min at a flow rate of 200 nl/min. Mass spectrometry analysis was performed on a Q-Exactive HF mass spectrometer equipped with a nanoelectrospray ion source (both Thermo Fisher Scientific). Each MS1 scan was followed by high-collision-dissociation (HCD) of the 10 most abundant precursor ions with dynamic exclusion for 20 s. The total cycle time was approximately 1 s. For MS1, $3e^6$ ions were accumulated in the Orbitrap cell over a maximum time of 100 ms and scanned at a resolution of 120,000 full width at half-maximum (FWHM) (at 200 m^*z^{-1}). MS2 scans were acquired at a target setting of $1e^5$ ions, accumulation

time of 50 ms, and a resolution of 30,000 FWHM (at 200 m/z^{-1}). Singly charged ions and ions with unassigned charge state were excluded from triggering MS2 events. The normalized collision energy was set to 28%, the mass isolation window was set to 1.4 $m*z^{-1}$, and one microscan was acquired for each spectrum.

The acquired raw files were searched against a yeast database (UniProt: download date: 30/10/2014, total of 6652 entries) by MaxQuant software (version 1.0.13.13) using default parameters. The best six transitions for each peptide were selected automatically using an in-house software tool and imported to Spectrodive software (version 10.0). Mass isolation lists containing six peptides for the target protein were exported from Spectrodive and imported into the Orbitrap Fusion Lumos operating software for SureQuant analysis. Chromatographic separation of peptides was carried out using an EASY nano-LC 1200 system (Thermo Fisher Scientific) equipped with a heated RP-HPLC column (75 µm × 37 cm) packed in-house with 1.9 µm C18 resin (Reprosil-AQ Pur; Dr. Maisch). For SureQuant analysis, peptide samples were spiked with the heavy reference peptide mix at 10 fmol/peptide/µg of total peptide mass. The peptides were separated using a following linear gradient: from 95% solvent A (0.1% formic acid in water [vol/vol]) and 5% solvent B (80% acetonitrile, 19.9% water, 0.1% formic acid [vol/vol/vol]) to 45% solvent B over 60 min at the constant flow rate of 200 nl/min. MS data were acquired with the following settings: The resolution of the Orbitrap was set to 30,000 (120,000) FWHM (at 200 m/z) for heavy (light) peptide ions, and the fill time was set to 54 (246) ms, respectively, to reach a target value of 1×10^6 ions. The ion isolation window was set to 0.4 m/z, and the scan range was set to 150–1500 m/z. The mass window for triggering heavy PRM scans was set to 10 ppm, and the depended PRM triggering threshold for the light channel was set to a minimum of two detected transitions. For each MS cycle, a full MS1 scan at 120,000 FWHM (at 200 m/z) was included. In addition, a few selected samples were also analyzed in DDA mode using the same LC gradient and parameters as above.

For the quantitative analysis, the PRM files were imported and processed using Spectrodive software with the SureQuant default settings. For each target peptide, the total peak areas of the most intense transitions were exported. Only peptides with the Elution Group Q.Value <0.01 were considered for quantitative analysis. To control for variation in sample amounts, the total ion chromatogram (comprising only peptide ions with two or more charges) of each sample was determined by Progenensis QI (version 2.0; Waters) and used for normalization. In addition, as the alternative normalization approach, the raw files were imported into Skyline software (version 4.2) to extract and sum the MS1 intensities of peptide ions belonging to constitutively expressed proteins (glyceraldehyde-3-phosphate dehydrogenase 3, enolase 2, and actin; two peptides for each protein were selected). PRM (MS2) intensities of target peptides were then normalized to the summed (MS1) intensity of selected peptides from the constitutively expressed proteins.

Mass spectrometry analyses of a tryptic digest of YPD medium

Lysis buffer (80 µl) (8 M urea [Sigma], 100 mM ammonium bicarbonate) was added to 20 µl of YPD medium. Samples were sonicated using a Bioruptor (10 cycles, 30 s on/off; Diagenode). Proteins were reduced with 5 mM Tris(2-carboxyethyl)phosphine (TCEP) for 60 min at 37°C and alkylated with 10 mM chloroacetamide for 30 min at 37°C. Urea was diluted with 100 mM ammonium bicarbonate to the final concentration of 1.6 M, and proteins were digested with sequencing-grade modified trypsin (1/50, wt/wt; Promega, Madison, WI) overnight at 37°C. Samples were then acidified with 5% TFA, and peptides were desalted on C18 reversed-phase spin columns according to the manufacturer's instructions (Macrospin; Harvard Apparatus). The eluate fraction was dried under vacuum and reconstituted with 0.1% formic acid to 0.5 µg/µl peptide concentration. MS analysis was performed as described above.

Gaussian process regression for mass spectrometry data

The mass spectrometry measurements of Cln3 of Litsios *et al.* (2019) were smoothed using Gaussian processes (GP) regression (further details on this method can be found in Litsios *et al.*, 2019). We used a GP with zero prior mean and a rational quadratic covariance function and assumed that each measurement was corrupted by additive Gaussian noise with unknown variance. The measurements from all replicates that passed the quality criteria at each time point were used together in the GP smoothing process, so that the smoothing algorithm would correctly account for the variability present in the measurements. The hyperparameters of the GP covariance function and the measurement noise variance were estimated by maximizing the marginal likelihood of the measurements using multistart optimization started from 20 random initial points. At the end of this step, an optimized posterior GP was obtained. The mean and SD of this posterior GP was evaluated over a dense grid of time points to generate Figure 6D.

Quantification of Western blot data

ImageJ software (v.1.52n; Java 1.8.0_202) was used to quantify the bands in the Western blot images of Lucena *et al.* (2018). After converting the images to grayscale, we selected a region of interest (ROI) corresponding to the largest protein band across the row and measured the mean gray value of the protein of interest (POI) as well as the loading control (LC) and the background (BC). The latter was measured below or above each band where no stain is present on the blot. To obtain the background-corrected value for each POI and LC, the BC corresponding to each band was subtracted. Finally, for each time point the POI/LC ratio was calculated and plotted.

ACKNOWLEDGMENTS

We thank Liesbeth Veenhoff for the Nup133-yeGFP strain. This work was supported by grants from the Dutch Research Council (NWO) to M.H. (VICI, VI.C.192.003) and to A.M.-A. (VIDI, 016.Vidi.189.116), the National Science Foundation (NSF PHY 1806638) to C.A.R., the Sigrid Jusélius foundation to S.T., and the Canadian Institutes of Health Research (FDN-167277) to M.T.

REFERENCES

Ahrné E, Glatter T, Viganò C, von Schubert C, Nigg EA, Schmidt A (2016). Evaluation and improvement of quantification accuracy in isobaric mass tag-based protein quantification experiments. J Proteome Res 15, 2537–2547.

Barber F, Amir A, Murray AW, Murray AW (2020). Cell-size regulation in budding yeast does not depend on linear accumulation of Whi5. Proc Natl Acad Sci USA 117, 14243–14250.

Bhatta H, Goldys EM, Ma J (2006). Fluorescence and fluorescence-lifetime imaging microscopy (FLIM) to characterize yeast strains by autofluorescence. In: Imaging, Manipulation, and Analysis of Biomolecules, Cells, and Tissues IV, International Society for Optics and Photonics, 608801.

Black L, Tollis S, Fu G, Fiche JB, Dorsey S, Cheng J, Ghazal G, Notley S, Crevier B, Bigness J, *et al.* (2020). G1/S transcription factors assemble in increasing numbers of discrete clusters through G1 phase. J Cell Biol 219, e202003041.

Blank HM, Callahan M, Pistikopoulos IPE, Polymenis AO, Polymenis M (2018). Scaling of G1 duration with population doubling time by a cyclin in Saccharomyces cerevisiae. Genetics 210, 895–906.

Bourges AC, Torres Montaguth OE, Ghosh A, Tadesse WM, Declerck N, Aertsen A, Royer CA (2017). High pressure activation of the Mrr

restriction endonuclease in Escherichia coli involves tetramer dissociation. Nucleic Acids Res 45, 5323–5332.
Bradski G (2000). The opencv library. Dr Dobb's J Softw Tools 25, 120–125.
Campbell K, Westholm J, Kasvandik S, Di Bartolomeo F, Mormino M, Nielsen J (2020). Building blocks are synthesized on demand during the yeast cell cycle. Proc Natl Acad Sci USA 117, 7575–7583.
Chen Y, Zhao G, Zahumensky J, Honey S, Futcher B (2020). Differential scaling of gene expression with cell size may explain size control in budding yeast. Mol Cell 78, 359–370.e6.
Costanzo M, Nishikawa JL, Tang X, Millman JS, Schub O, Breitkreuz K, Dewar D, Rupes I, Andrews B, Tyers M (2004). CDK activity antagonizes Whi5, an inhibitor of G1/S transcription in yeast. Cell 117, 899–913.
Cranfill PJ, Sell BR, Baird MA, Allen JR, Lavagnino Z, De Gruiter HM, Kremers GJ, Davidson MW, Ustione A, Piston DW (2016). Quantitative assessment of fluorescent proteins. Nat Methods 13, 557–562.
Cutrale F, Rodriguez D, Hortigüela V, Chiu CL, Otterstrom J, Mieruszynski S, Seriola A, Larrañaga E, Raya A, Lakadamyali M, *et al.* (2019). Using enhanced number and brightness to measure protein oligomerization dynamics in live cells. Nat Protoc 14, 616–638.
De Bruin RAM, McDonald WH, Kalashnikova TI, Yates J, Wittenberg C (2004). Cln3 activates G1-specific transcription via phosphorylation of the SBF bound repressor Whi5. Cell 117, 887–898.
Dorsey S, Tollis S, Cheng J, Black L, Notley S, Tyers M, Royer CA (2018). G1/S transcription factor copy number is a growth-dependent determinant of cell cycle commitment in yeast. Cell Syst 6, 539–554.e11.
Dreier RF, Ahrné E, Broz P, Schmidt A (2018). Global ion suppression limits the potential of mass spectrometry based phosphoproteomics. J Proteome Res 18, 493–507.
Fadero TC, Gerbich TM, Rana K, Suzuki A, DiSalvo M, Schaefer KN, Heppert JK, Boothby TC, Goldstein B, Peifer M, *et al.* (2018). LITE microscopy: tilted light-sheet excitation of model organisms offers high resolution and low photobleaching. J Cell Biol 217, 1869–1882.
Ferrezuelo F, Colomina N, Palmisano A, Garí E, Gallego C, Csikász-Nagy A, Aldea M (2012). The critical size is set at a single-cell level by growth rate to attain homeostasis and adaptation. Nat Commun 3, 1012.
Garmendia-Torres C, Tassy O, Matifas A, Molina N, Charvin G (2018). Multiple inputs ensure yeast cell size homeostasis during cell cycle progression. eLife 7, e34025.
Gordon A, Colman-Lerner A, Chin TE, Benjamin KR, Yu RC, Brent R (2007). Single-cell quantification of molecules and rates using open-source microscope-based cytometry. Nat Methods 4, 175–181.
Harris MR, Lee D, Farmer S, Lowndes NF, de Bruin RAM (2013). Binding specificity of the G1/S transcriptional regulators in budding yeast. PLoS One 8, e61059.
Hellriegel C, Caiolfa VR, Corti V, Sidenius N, Zamai M (2011). Number and brightness image analysis reveals ATF-induced dimerization kinetics of uPAR in the cell membrane. FASEB J 25, 2883–2897.
Joglekar AP, Salmon ED, Bloom KS (2008). Counting kinetochore protein numbers in budding yeast using genetically encoded fluorescent proteins. Methods Cell Biol 85, 127–151.
Jorgensen P, Edgington NP, Schneider BL, Rupeš I, Tyers M, Futcher B (2007). The size of the nucleus increases as yeast cells grow. Mol Biol Cell 18, 3523–3532.
Jorgensen P, Nishikawa JL, Breitkreutz BJ, Tyers M (2002). Systematic identification of pathways that couple cell growth and division in yeast. Science 297, 395–400.
Kanshin E, Tyers M, Thibault P (2015). Sample collection method bias effects in quantitative phosphoproteomics. J Proteome Res 14, 2998–3004.
Lakowicz JR, Szmacinski H, Nowaczyk K, Johnson ML (1992). Fluorescence lifetime imaging of free and protein-bound NADH. Proc Natl Acad Sci USA 89, 1271–1275.
Litsios A, Huberts DHEW, Terpstra HM, Guerra P, Schmidt A, Buczak K, Papagiannakis A, Rovetta M, Hekelaar J, Hubmann G (2019). Differential scaling between G1 protein production and cell size dynamics promotes commitment to the cell division cycle in budding yeast. Nat Cell Biol 21, 1382–1392.
Lo CA, Kays I, Emran F, Lin TJ, Cvetkovska V, Chen BE (2015). Quantification of protein levels in single living cells. Cell Rep 13, 2634–2644.
Lucena R, Alcaide-Gavilán M, Schubert K, He M, Domnauer MG, Marquer C, Klose C, Surma MA, Kellogg DR (2018). Cell size and growth rate are modulated by TORC2-dependent signals. Curr Biol 28, 196–210.
Maltas J, Amer L, Long Z, Palo D, Oliva A, Folz J, Urayama P (2015). Autofluorescence from NADH conformations associated with different metabolic pathways monitored using nanosecond-gated spectroscopy and spectral phasor analysis. Anal Chem 87, 5117–5124.
Moutin E, Compan V, Raynaud F, Clerté C, Bouquier N, Labesse G, Ferguson MLML, Fagni L, Royer CACA, Perroy J (2014). The stoichiometry of scaffold complexes in living neurons—DLC2 functions as a dimerization engine for GKAP. J Cell Sci 127, 3451–3462.
Nagy P, Claus J, Jovin TM, Arndt-Jovin DJ (2010). Distribution of resting and ligand-bound ErbB1 and ErbB2 receptor tyrosine kinases in living cells using number and brightness analysis. Proc Natl Acad Sci USA 107, 16524–16529.
Peterson AC, Russell JD, Bailey DJ, Westphall MS, Coon JJ (2012). Parallel reaction monitoring for high resolution and high mass accuracy quantitative, targeted proteomics. Mol Cell Proteom 11, 1475–1488.
Qu Y, Jiang J, Liu X, Wei P, Yang X, Tang C (2019). Cell cycle inhibitor Whi5 records environmental information to coordinate growth and division in yeast. Cell Rep 29, 987–994.e5.
Rosebrock AP (2017). Synchronization of budding yeast by centrifugal elutriation. Cold Spring Harb Protoc 2017, pdb.prot088732.
Schmoller KM, Turner JJ, Koivomagi M, Skotheim JM (2015). Dilution of the cell cycle inhibitor Whi5 controls budding-yeast cell size. Nature 526, 268–272.
Soifer I, Barkai N (2014). Systematic identification of cell size regulators in budding yeast. Mol Syst Biol 10, 761.
Sommer RA, Dewitt JT, Tan R, Kellogg DR (2021). Growth-dependent signals drive an increase in early g1 cyclin concentration to link cell cycle entry with cell growth. eLife 10, e64364.
Talarek N, Gueydon E, Schwob E (2017). Homeostatic control of START through negative feedback between Cln3-Cdk1 and Rim15/Greatwall kinase in budding yeast. eLife 6, e26233.
Thorburn RR, Gonzalez C, Brar GA, Christen S, Carlile TM, Ingolia NT, Sauer U, Weissman JS, Amon A (2013). Aneuploid yeast strains exhibit defects in cell growth and passage through START. Mol Biol Cell 24, 1274–1289.
Verdaasdonk JS, Lawrimore J, Bloom K (2014). Determining absolute protein numbers by quantitative fluorescence microscopy. Methods Cell Biol 123, 347–365.
Verduyn C, Postma E, Scheffers WA, Van Dijken JP (1992). Effect of benzoic acid on metabolic fluxes in yeasts: a continuous-culture study on the regulation of respiration and alcoholic fermentation. Yeast 8, 501–517.
Wagner MV, Smolka MB, de Bruin RAM, Zhou H, Wittenberg C, Dowdy SF (2009). Whi5 regulation by site specific CDK-phosphorylation in Saccharomyces cerevisiae. PLoS One 4, e4300.
Wang H, Carey LB, Cai Y, Wijnen H, Futcher B (2009). Recruitment of Cln3 cyclin to promoters controls cell cycle entry via histone deacetylase and other targets. PLoS Biol 7, e1000189.
Winston F, Dollard C, Ricupero-Hovasse SL (1995). Construction of a set of convenient Saccharomyces cerevisiae strains that are isogenic to S288C. Yeast 11, 53–55.
Zamai M, Trullo A, Giordano M, Corti V, Cuesta EA, Francavilla C, Cavallaro U, Caiolfa VR (2019). Number and brightness analysis reveals that NCAM and FGF2 elicit different assembly and dynamics of FGFR1 in live cells. J Cell Sci 132, jcs220624.
Zapata J, Dephoure N, MacDonough T, Yu Y, Parnell EJ, Mooring M, Gygi SP, Stillman DJ, Kellogg DR (2014). $PP2A^{Rts1}$ is a master regulator of pathways that control cell size. J Cell Biol 204, 359–376.
Zhang J, Schneider C, Ottmers L, Rodriguez R, Day A, Markwardt J, Schneider BL (2002). Genomic scale mutant hunt identifies cell size homeostasis genes in S. cerevisiae. Curr Biol 12, 1992–2001.